

Transition from weak- to strong-field coherent control

Carlos Trallero-Herrero and Thomas C. Weinacht

Department of Physics, Stony Brook University, Stony Brook, New York 11794, USA

(Received 13 December 2006; published 1 June 2007)

We trace out the transition from weak- to strong-field coherent control, focusing on multiphoton population transfer in atomic sodium. We show how dynamic Stark shifts and ground-state depletion mark the departure from perturbative to strong-field excitation, and how a time-domain picture yields insight into the dynamics when a static resonance, frequency-domain approach breaks down. Experimental measurements are interpreted with the help of calculations that numerically integrate the Schrödinger equation.

DOI: [10.1103/PhysRevA.75.063401](https://doi.org/10.1103/PhysRevA.75.063401)

PACS number(s): 32.80.Qk

I. INTRODUCTION

As the number of coherent control experiments has grown rapidly in the past several years, there has been increasing interest in strong-field control using shaped ultrafast laser pulses [1–10]. Shaped ultrafast laser pulses offer immense possibilities for control, with most current experiments allowing for programmable control over the phase and amplitude of over 100 frequency components. These pulses can be used to generate strong fields, which, while making the control more powerful, often makes the design and interpretation of optimal pulses (i.e., producing the maximum desired final-state amplitude for a given pulse energy) more complicated and difficult.

Closed-loop learning control experiments can overcome the design problem by using a learning algorithm in conjunction with experimental feedback to discover optimal pulse shapes for control [1,11,12]. However, while a few experiments have demonstrated that it is possible [13–16], interpreting the optimal pulse shapes discovered by a learning algorithm and understanding the strong-field dynamics underlying control is a challenging task. An important parallel approach is to try and take the intuition and insight that has been developed for the design of optimal pulses in a weak field and modify it to accommodate increasing intensities, where strong-field dynamics lead to a breakdown of weak-field predictions [2]. This approach has already led to success in finding solutions that maintain selectivity, although not efficiency (i.e., population inversion) in strong fields. In this paper we address the question of efficient excitation in strong fields and trace out the transition from weak- to strong-field coherent control in a simple atomic system. We address what we consider to be general features of strong-field control. In particular, we note that, while a frequency-domain picture is appropriate for weak field, or perturbative control [17–20], it inherently breaks down as one moves to the strong-field regime. In strong fields, dynamic Stark shifts (DSSs) render all resonances *dynamic* [1,2,21,22], with time-independent resonances no longer dictating optimal control parameters. In this case, a time-domain phase-matching picture is very useful for understanding the control dynamics [16]. We illustrate how closed-loop control can accommodate strong fields, and then we focus on parametrized pulse shape scans which can be interpreted for both weak and strong fields, yielding a detailed understanding of the transition from weak- to strong-field control.

The paper is broken down into three sections: the theoretical background, the experimental apparatus, and the results and discussion. In Sec. II, we discuss what quantities define the weak- and strong-field regimes and derive an analytic expression that illustrates the time-domain interpretation of the strong-field results. Section III contains a description of the experimental apparatus, and Section IV presents our experimental results and interprets them with the help of calculations.

II. THEORY

Recent experiments have focused on multiphoton excitation in the limit of weak fields [18–20]. In this limit, perturbation theory can be used to calculate the pulse shape dependence of multiphoton excitation and yields excellent agreement with experimental measurements. However, in general, a perturbative treatment of the interaction between the light field and atomic system is not sufficient and does not adequately describe the atom-field dynamics. We start by summarizing the results of perturbation theory describing the multiphoton coupling of two and three atomic levels. We then provide the results of a more general calculation [23], illustrating what conditions are necessary to recover, and therefore define, the weak-field limit.

A. Perturbative multiphoton absorption

We first consider a two-photon transition with no intermediate resonances [24]. If the detuning of the intermediate states is large, they will not be populated by the pulse and the process can be described by a simple two-level Hamiltonian. In the rotating-wave approximation (RWA), a second-order perturbation theory calculation yields the following result for the excited-state amplitude $a_e(t)$ [18]:

$$a_e(t) = -\frac{1}{\hbar^2} \sum_m \mu_{em} \mu_{mg} \int_{-\infty}^t \int_{-\infty}^{t_1} \varepsilon(t_1) \varepsilon(t_2) \times \exp(-i\Delta_{em}t_1) \exp(-i\Delta_{mg}t_2) dt_1 dt_2, \quad (1)$$

where $\varepsilon(t) = \varepsilon_0 \sqrt{g(t)} e^{i\varphi(t)/2}$ is the electric field, ω_0 is the laser frequency, $\Delta_{ij} = \omega_0 - \omega_{ij}$, $\omega_{ij} = \omega_i - \omega_j$, and $\hbar\omega_i$ is the i th state energy. Performing the inner integral for large detuning of intermediate states, where $\exp(-i\Delta_{mg}t_2)$ varies rapidly com-

pared to $\varepsilon(t_2)$, and taking the limit $t \rightarrow \infty$ [18], we obtain the two-photon absorption (TPA) probability,

$$P_{g \rightarrow e} = \left| \frac{\langle e | \mu^2 | g \rangle}{\bar{\omega} \hbar^2} \right|^2 \left| \int_{-\infty}^{\infty} \varepsilon^2(t) \exp(-i\Delta t) dt \right|. \quad (2)$$

Here $\Delta = 2\omega_0 - \omega_{eg}$, $\hbar\omega_e$ and $\hbar\omega_g$ are the excited- and ground-state energies, respectively, $\hbar\bar{\omega}$ is an appropriately weighted average energy of parity-allowed far-detuned intermediate states, and $\langle e | \mu^2 | g \rangle$ is the effective two-photon coupling [18]. In the field parametrization above, $g(t)$ is the intensity envelope (Gaussian), and $\varphi(t)/2$ is the phase of the field. This result can easily be generalized to an N th-order process [18]. In the frequency domain Eq. (2) can be rewritten as

$$P_{g \rightarrow e} \propto \left| \int_{-\infty}^{\infty} \tilde{\varepsilon}(\omega_{eg}/2 + \Omega) \tilde{\varepsilon}(\omega_{eg}/2 - \Omega) d\Omega \right|^2 \propto \left| \int_{-\infty}^{\infty} A(\omega_{eg}/2 + \Omega) A(\omega_{eg}/2 - \Omega) \times e^{i[\Phi(\omega_{eg}/2 + \Omega) + \Phi(\omega_{eg}/2 - \Omega)]} d\Omega \right|^2, \quad (3)$$

where $\varepsilon(\omega) = A(\omega)e^{i\Phi(\omega)}$ is the Fourier transform of $\varepsilon(t)$. $A(\omega)$ and $\Phi(\omega)$ are the spectral amplitude and phase, respectively. From this last expression, the transition probability can be interpreted in terms of a sum over photon pairs that satisfy the resonance condition $\omega_1 + \omega_2 = \omega_{eg}$. The two most important points in the weak-field limit, in the context of this work, are the following. First, the resonance condition governing the transition probability is static (time independent) and a frequency-domain interpretation of control is natural. Second, while there are an infinite number of optimal pulse shapes (those with antisymmetric spectral phase), pulse shaping is not required to optimize population transfer. By contrast, if there is an intermediate resonance en route to the final state, then pulse shaping is required to optimize population transfer to the final state [25]. A generalization of the perturbative expression above describes the case of (2+1)-resonance-mediated three-photon absorption. This is a natural case to examine as an extension to the nonresonant two-photon case because it combines the simplest nonresonant multiphoton case with a resonance enhancement involving the minimum number of states. Recent work has focused on control of resonance-mediated three-photon (2+1) absorption in the weak-field limit [20].

Using again the RWA, third-order perturbation theory yields the following expression for the probability amplitude a_r of the third state, resonantly coupled to the intermediate level (the excited state a_e in the discussion above):

$$a_r(t) = -\frac{1}{i\hbar^3} \sum_m \mu_{re} \mu_{em} \mu_{mg} \int_{-\infty}^t \int_{-\infty}^{t_1} \int_{-\infty}^{t_2} \varepsilon(t_1) \varepsilon(t_2) \varepsilon(t_3) \times \exp(-i\Delta_{re}t_1) \exp(-i\Delta_{em}t_2) \exp(-i\Delta_{mg}t_3) dt_1 dt_2 dt_3. \quad (4)$$

Note the similarity between Eqs. (1) and (4). As in the TPA case, the innermost integral can be performed explicitly assuming large detuning of the intermediate states for the two-photon transition. We separate different contributions for excitation to the r state based on whether or not they involve a resonance enhancement from the intermediate state e . Details are given in Refs. [20,25]. The final-state amplitude in terms of resonant and near-resonant contributions is

$$a_r \propto (a_r^{on \text{ res}} + a_r^{near \text{ res}}),$$

$$a_r^{on \text{ res}} = i\pi \varepsilon(\omega) \int_{-\infty}^{\infty} \varepsilon(\omega') \varepsilon(\omega_{eg} - \omega) d\omega,$$

$$a_r^{near \text{ res}} = \int_{-\infty}^{\infty} \varepsilon(\omega) P \int_{-\infty}^{\infty} \frac{\varepsilon(\omega') \varepsilon(\omega_{rg} - \omega - \omega')}{\omega_{eg} - (\omega + \omega')} d\omega' d\omega, \quad (5)$$

with P being the Cauchy principal value operator [20]. $a_r^{on \text{ res}}$ contains the contribution to a_r from frequency combinations that are resonant with the intermediate level and $a_r^{near \text{ res}}$ contains all other contributions.

B. Strong-field excitation and recovering the perturbative limit

In order to include excitation with electric fields that result in a nonperturbative interaction, we move to a more general treatment outlined in earlier publications [16,23]. We first discuss the two-level case in detail and then briefly indicate how the analysis carries over to the case of three levels and the perturbative limit is recovered in the case of an intermediate resonance. As in the cases discussed above, we consider a nonresonant two-photon transition within the RWA. The far-detuned intermediate states can be integrated explicitly using an adiabatic approximation. The strong-field two-level atom-field Hamiltonian can be written as

$$\hat{\mathbf{H}}(t) = \begin{pmatrix} \omega_g^{(s)}(t) & \chi(t) e^{i[\Delta t - \varphi(t)]} \\ \chi(t) e^{-i[\Delta t - \varphi(t)]} & \omega_e^{(s)}(t) \end{pmatrix}. \quad (6)$$

Here $\Delta = 2\omega_0 - \omega_{eg}$ is the two-photon atom-field detuning and $\omega_g^{(s)}(t)$ and $\omega_e^{(s)}(t)$ represent the time-varying DSSs of the ground and excited states, respectively,

$$\omega_{\{e,g\}}^{(s)}(t) = -\sum_m \frac{\mu_{\{e,g\}m}^2 I_0 g(t)}{\hbar^2 c \epsilon_0} \frac{\omega_{m\{e,g\}}}{\omega_{m\{e,g\}}^2 - \omega_0^2} = -\sum_m \frac{\mu_{\{e,g\}m}^2 \varepsilon_0^2 g^2(t)}{2\hbar^2} \frac{\omega_{m\{e,g\}}}{\omega_{m\{e,g\}}^2 - \omega_0^2}, \quad (7)$$

$$I(t) = \frac{1}{2} \epsilon_0 c |\varepsilon(t)|^2 = I_0 g(t). \quad (8)$$

ϵ_0 is the free-space electric permittivity and c the speed of light. $\chi(t)$ is the two-photon Rabi frequency,

$$\chi(t) = - \sum_m \frac{\mu_{em}\mu_{mg}}{(2\hbar)^2} \frac{\varepsilon_0^2 g(t)}{\omega_{mg} - \omega_0}. \quad (9)$$

This form of the Hamiltonian highlights the fact that, in strong fields, DSSs of the ground and excited states result in a changing resonance condition as the intensity of the laser pulse rises and falls, since $\omega_{e,g}^{(s)} \propto I(t)$. $\hat{\mathbf{H}}(t)$ can be transformed to transfer the phase in the coupling to the diagonal terms, which illustrates how to compensate for the DSSs. By using the transformation

$$\begin{aligned} a_g(t) &= b_g(t) e^{i(\Delta t - \varphi)/2} e^{-i(2) \int_{-\infty}^t [\omega_e^{(s)}(t') + \omega_g^{(s)}(t')] dt'}, \\ a_e(t) &= b_e(t) e^{-i(\Delta t - \varphi)/2} e^{-i(2) \int_{-\infty}^t [\omega_e^{(s)}(t') + \omega_g^{(s)}(t')] dt'}, \end{aligned} \quad (10)$$

where $a_g(t)$ and $a_e(t)$ are the amplitudes for the ground and excited states, respectively, we arrive at the Hamiltonian $\hat{\mathbf{H}} \rightarrow \hat{\mathbf{H}}'$,

$$\hat{\mathbf{H}}' = \begin{pmatrix} -\frac{1}{2} [\delta_\omega^{(s)}(t) - \Delta + \dot{\varphi}(t)] & \chi(t) \\ \chi(t) & \frac{1}{2} [\delta_\omega^{(s)}(t) - \Delta + \dot{\varphi}(t)] \end{pmatrix}, \quad (11)$$

where the physically relevant differential Stark shift is defined as

$$\delta_\omega^{(s)}(t) = \omega_e^{(s)}(t) - \omega_g^{(s)}(t). \quad (12)$$

Maintaining resonance (diagonal terms equal to zero in the Hamiltonian) can be accomplished by tailoring the laser phase $\varphi(t)$ in order to compensate for the DSSs. The diagonal elements in the Hamiltonian Eq. (11) lead us to define the quantity

$$\alpha(t) = - \left(\int_{-\infty}^t \delta_\omega^{(s)}(t') dt' - \Delta t + \varphi(t) \right), \quad (13)$$

which is particularly useful for describing optimal excitation conditions in the strong-field limit. $\alpha(t)$ can be interpreted in terms of an atom-field phase. Keeping this phase constant (i.e., phase locking) is equivalent to maintaining resonance despite movement of the atomic levels in the strong field of the laser. It can be accomplished by balancing the atomic phase accumulated through dynamic Stark shifts with a tailored temporal laser phase. In order to arrive at an explicit expression for the optimal pulse shape in this general case, we transform the Hamiltonian of Eq. (11) once more:

$$\begin{aligned} b_g(t) &= c_g(t) e^{-i\alpha(t)/2}, \\ b_e(t) &= c_e(t) e^{i\alpha(t)/2}. \end{aligned} \quad (14)$$

We arrive at

$$\hat{\mathbf{H}}'' = \begin{pmatrix} 0 & \chi(t) e^{i\alpha(t)} \\ \chi(t) e^{-i\alpha(t)} & 0 \end{pmatrix}, \quad (15)$$

from which the strong-field π pulse condition is evident [26]:

$$\int_{-\infty}^{\infty} \chi(t) \exp[i\alpha(t)] dt = \frac{\pi}{2}. \quad (16)$$

This last equation makes clear the role of $\alpha(t)$ [Eq. (13)] in determining the population transfer for a given pulse shape. If $\alpha(t)$ evolves rapidly while the coupling $\chi(t)$ is significant, then the integral given in Eq. (16) will vanish as the atom-laser phase oscillates. Oscillation of the atom-laser phase corresponds to an oscillation between stimulated emission and absorption, and they can cancel each other out to result in essentially zero net population transfer. Controlling the laser phase $\varphi(t)$ allows for minimizing the variation of $\alpha(t)$ during the pulse, and therefore maximizing the population transfer. This is equivalent to maintaining resonance by dynamically following the instantaneous energy separation of the ground- and excited-state levels.

Clearly, the weak-field limit of this general case imposes conditions, not only on the excited-state amplitude, but also on the DSSs of the ground and excited states. To illustrate this, we start with the Hamiltonian of Eq. (15) and show that only in the limit of vanishing excited-state amplitude *and* dynamic Stark shift,

$$\delta_\omega^{(s)} \approx 0,$$

$$|a_g(t)| \approx 1 \quad (17)$$

does one recover the perturbative limit Eq. (2). For simplicity, we consider the case of zero two-photon detuning $\Delta=0$. Using the Hamiltonian Eq. (15), the Schrödinger equation for amplitude c_e is

$$\dot{c}_e(t) = i\chi_0 \int_{-\infty}^{\infty} \varepsilon(t)^2 e^{-i \int_{-\infty}^t \delta_\omega^{(s)}(t') dt'} c_g(t) dt, \quad (18)$$

with (see [23])

$$\chi_0 = - \sum_m \frac{\mu_{em}\mu_{mg}}{(2\hbar)^2} \frac{1}{\omega_{mg} - \omega_0}. \quad (19)$$

Only by taking the limit of a vanishing differential Stark shift and excited-state population [Eq. (17)] can we arrive at the following result which agrees with the perturbation theory results given by Eq. (2):

$$|a_e(t)|^2 = |c_e(t)|^2 = P_{g \rightarrow e} = |\chi_0|^2 \left| \int_{-\infty}^{\infty} \varepsilon(t)^2 \exp(i\Delta t) dt \right|^2. \quad (20)$$

The extension of the two-level Hamiltonian to the case of a three-level system where the third level is resonantly coupled to the excited state and dipole allowed is simple:

$$\hat{\mathbf{H}}_3(t) = \begin{pmatrix} \omega_g^{(s)}(t) & \chi^*(t)e^{i[\Delta t - \varphi(t)]} & 0 \\ \chi(t)e^{-i[\Delta t - \varphi(t)]} & \omega_e^{(s)}(t) & \chi_{er}^*(t)e^{-i[\varphi(t)/2 - \Delta_{er}t]} \\ 0 & \chi_{er}(t)e^{i[\varphi(t)/2 - \Delta_{er}t]} & \omega_r^{(s)}(t) \end{pmatrix} \quad (21)$$

with

$$\chi_{er}(t) = \frac{\mu_{re}}{2\hbar} \varepsilon(t). \quad (22)$$

Here, μ_{re} and Δ_{er} are the one-photon coupling between the excited and resonant states and the detuning. $\omega_r^{(s)}(t)$ is the DSS of the final (r) state. As in the two-level case, the perturbative solution Eq. (5) can be recovered from the general Hamiltonian Eq. (21) in the same limit that the ground state is not depleted [$|a_g(t)| \approx 1$] and the Stark shifts vanish [$\delta_\omega^{(s)} \approx 0$, $\omega_r^{(s)}(t) \approx 0$]. The evolution of the intermediate- and final-state amplitudes a_e and a_r in this limit are given by

$$\dot{a}_e(t) = i\chi(t)e^{-i[\Delta t - \varphi(t)]}, \quad (23)$$

$$\dot{a}_r(t) = i\chi_{er}(t)e^{i[\varphi(t)/2 - \Delta_{er}t]}a_e(t). \quad (24)$$

We can integrate these two equations explicitly, giving

$$a_r(t) = - \int_{-\infty}^t dt' \int_{-\infty}^{t'} dt'' \chi_{er}(t') e^{i[\varphi(t')/2 - \Delta_{er}t']} \chi(t'') e^{-i[\Delta t'' - \varphi(t'')]} \quad (25)$$

Taking the limit $t \rightarrow \infty$, substituting for the Rabi frequencies, and expressing the fields in terms of Fourier integrals, we recover the weak limit Eq. (5) [20,25]:

$$a_r^{on\ res} = i\pi \varepsilon(\omega) \int_{-\infty}^{\infty} \varepsilon(\omega) \varepsilon(\omega_{eg} - \omega) d\omega, \\ a_r^{near\ res} = \int_{-\infty}^{\infty} \varepsilon(\omega) \mathcal{P} \int_{-\infty}^{\infty} \frac{\varepsilon(\omega') \varepsilon(\omega_{eg} - \omega - \omega')}{\omega_{eg} - (\omega + \omega')} d\omega' d\omega. \quad (26)$$

Our numerical simulations involved integrating the three-level, time-dependent, Schrödinger equation with corresponding Hamiltonian Eq. (21) using a fourth-order Runge-Kutta approach. Table I shows the most significant values for dipole moments μ_{ij} , transition frequencies ω_{ij} , and contributions to the DSSs of the $4s$, $3s$, and $7p$ states. The three-level calculations were checked against calculations with the intermediate off-resonant states included explicitly.

III. EXPERIMENTAL APPARATUS

We carried out experiments using a femtosecond laser system capable of producing 30 fs pulses with 1 mJ of energy at a 1 kHz repetition rate. The central wavelength of the laser is around 780 nm, with a tunability of about 10 nm. A portion of the amplified pulses are directed into an acousto-

optic modulator (Brimrose, TeO₂ longitudinal mode, 150 MHz) based pulse shaper under computer control. The acoustic wave form is directly synthesized by an arbitrary wave-form generator (Gage Applied Sciences model CompuGen 11G) mounted on the PCI bus of the computer. The pulse energy following the pulse shaper is approximately 220 μ J. The pulse shaper is under computer control, allowing for both parametrized pulse shape scans as well as the use of our genetic algorithm (GA) for selecting pulse shapes. While our pulse shaper is capable of both phase and amplitude modulation, we restricted the pulse shaping in this work to phase only, in order to keep the pulse energy constant. The details of our GA have been reported previously [29]. Following the pulse shaper, the pulses were focused into a gold pinhole with a diameter of 100 μ m using a 1-m-focal-length lens. This limited intensity variation across the transverse profile of the beam to about 20%. The use of a long-focal-length lens is very important, since it avoids the presence of nonlinear optical processes at the focus. The apertured laser beam was imaged into a sodium heat pipe oven. This imaging system consisted of a 2 in., $f=75$ cm focal length lens with a magnification of 4. The magnification allowed us to maximize the number of atoms exposed to the laser while maintaining sufficient energy for a π pulse. The peak intensity at the focus in the heat pipe oven for an unshaped pulse was about 2.8×10^{11} W/cm².

The heat pipe oven contains a mixture of Na and Ar gas at temperatures around 290 °C. Na serves as an ideal system

TABLE I. Peak Stark shifts, dipole moments, and transition frequencies for the Na lines used in the calculations. All values are for center frequency $\omega_0=777$ nm and ideal π pulse intensity for a 50 fs field duration full width at half maximum. Stark shifts are calculated according to Eq. (7), and dipole moments are calculated from line strengths given in [27] according to [28].

Line	Dipole moment (10 ⁻²⁹ C m)	Transition frequency (10 ¹⁵ rad/s)	Stark shift (10 ¹² rad/s)
3s-3p	2.11	3.19	-16.1
3s-4p	0.189	5.70	-0.037
3s-5p	0.070	6.60	-0.004
4s-3p	2.09	1.65	-11.3
4s-4p	4.87	0.853	19.1
4s-5p	0.571	1.75	0.992
4s-6p	0.230	2.17	0.494
4s-7p	0.132	2.41	
4s-8p	0.089	2.55	-0.153
7p-5s	0.448	1.00	0.404
7p-6s	1.75	0.409	2.14
7p-5d	0.672	0.284	0.242

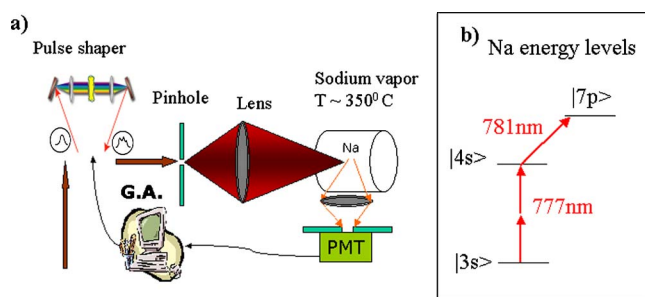


FIG. 1. (Color online) (a) Experimental setup. (b) Na energy levels.

for illustrating the transition to strong-field control. It has a simple electronic structure and the $3s$ - $4s$ and $4s$ - $7p$ transitions are two-photon and one-photon resonant at 777 and 781 nm, respectively. As a measure of the population in the $4s$ state following the pulse, we measured the fluorescence of the Na D lines ($D1$ and $D2$) $3p$ to $3s$ at 589 nm, whereas for the $7p$ we used the transition $6d$ to $3p$ at 470 nm [27]. The fluorescence was measured using a photo multiplier tube (PMT) with interference filters for wavelength selection. In order to limit intensity variation along the laser propagation axis, we imaged the laser focus onto the PMT and placed a small aperture in front of the PMT. The aperture size was chosen to be small compared to the distance over which the intensity distribution of the laser changed along the propagation axis. The experimental setup is shown in Fig. 1(a).

The use of this filtering system is crucial when working in the strong-field limit [16]. In order to illustrate the importance of spatial filtering, in Fig. 2 we show the integrated fluorescence from the $3p$ to $3s$ decay as a function of pulse energy with and without the pinhole. This figure shows the beginning of Rabi oscillations when using the pinhole whereas without the pinhole there is a monotonic increase in the fluorescence yield for all intensities. The maximum energy shown for the case of using the pinhole is determined by the damage threshold of the pinhole. The figure inset shows the spatial modes with (solid line) and without (dashed line) the use of the pinhole. With no spatial filtering, there is a Gauss-

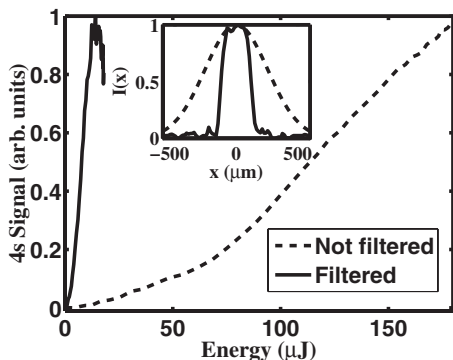


FIG. 2. $3p$ - $4s$ signal as function of energy for a spatially filtered beam and a Gaussian beam. The presence of Rabi oscillations is detected only when using the filtering system. Note that the signals for both the unfiltered and filtered laser beams are each normalized to themselves. Inset: filtered (solid line) and not filtered (dashed line) spatial profiles measured at the interaction region.

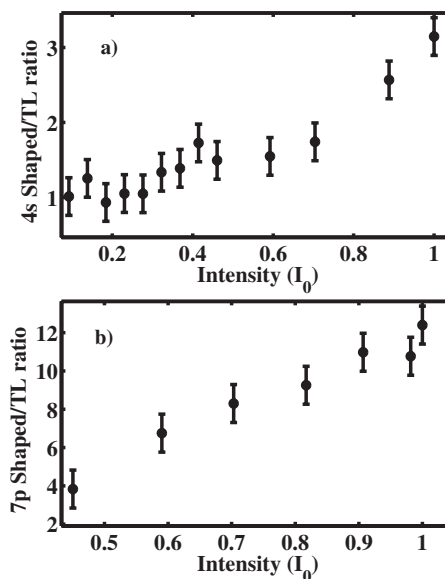


FIG. 3. (a) Ratio of $4s$ population for a GA maximized pulse to an unshaped one vs intensity. (b) Same as (a) but for the $7p$ state. I_0 is the peak intensity required for a π pulse on the $3s$ - $4s$ transition. Center wavelength is $\lambda_0=780$ nm. TL denotes transform limited (unshaped).

ian distribution of intensities in the interaction region, and the collected fluorescence originates from an ensemble of atoms exposed to a large range of laser intensities.

IV. RESULTS AND DISCUSSION

In order to illustrate how pulse shaping is required to maximize population transfer as one moves from the weak- to the strong-field regime, we used our GA to optimize the excitation to the $4s$ and $7p$ states at different laser pulse energies. Figures 3(a) and 3(b) show the ratio $P_{optimal}/P_{unshaped}$ for the $4s$ and $7p$ population transfers, respectively, as a function of pulse energy. $P_{optimal}$ is the population transfer obtained with a feedback-shaped pulse and $P_{unshaped}$ is the population transfer obtained with an unshaped pulse. There is a smooth transition from the weak- to strong-field regime, illustrated by the improvement in a shaped pulse relative to an unshaped one. The unshaped pulse becomes increasingly inadequate with increasing intensity and DSS, while the shaped pulse is able to compensate and maintain efficient population transfer [16]. Note that, in the weak-field limit, the ratio goes to 1 for the $3s$ - $4s$ transition, whereas the ratio goes to ~ 3 for the $3s$ - $7p$ transition. This highlights the fact that pulse shaping is required for optimizing population transfer even for weak fields if there is an intermediate resonance. The intensity I_0 corresponds to the peak intensity required for a π pulse on the $3s$ - $4s$ transition when compensating for the DSS. The ratio at high pulse energies is limited in part by our ability to eliminate spatial intensity averaging in the focus of the laser. Without the pinhole, the ratio would be about 1 for all intensities for the $4s$ population transfer. The error bars indicate the variation in population transfer for several optimizations at the same pulse energy.

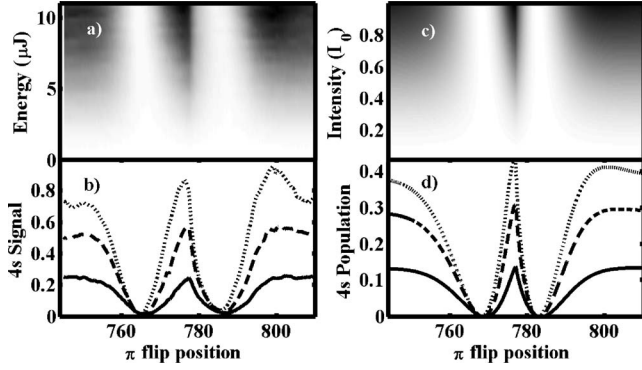


FIG. 4. (a) Experimental measurement of the $4s$ population as function of pulse energy (equivalent to peak intensity) and π flip position. (b) Lineouts of (a) for three different pulse energies. (c) Simulation of the $4s$ population as function of peak intensity and π flip position. (d) Lineouts of (c) for different intensities. The solid, dashed, and dotted lines are for $I=0.01I_0$, $0.5I_0$, and I_0 , respectively. The dark regions correspond to higher population transfer.

Measurements of the optimal pulse shapes (using second-harmonic generation frequency-resolved optical gating) for the $4s$ state confirm that the optimal pulses compensate for the DSSs [16]. The specific strategy developed by the learning algorithm depends on the detuning from the bare transition (777 nm), but all of the solutions were found to maximize $\int_{-\infty}^{\infty} \chi(t) \exp[i\alpha(t)] dt$.

In order to get a detailed picture of the change in dynamics going from the weak- to the strong-field regime, we performed a systematic study of the codependence on pulse shape and intensity for a simple and intuitive pulse shape parametrization—a π phase jump in the spectral phase. This pulse parametrization can be interpreted in both the weak- and strong-field regimes and provides a direct measure of the DSS as discussed below. For the case of the three-level system, a π phase jump around the intermediate resonance yields an intuitive enhancement over an unshaped pulse in the weak-field limit [20]. As there is a π phase shift of the response around resonance for a driven oscillator, one can improve the constructive interference of the near-resonance contributions to the three-photon $7p$ excitation by placing a π phase jump in the spectrum around the frequency resonant with the $4s$ - $7p$ transition. For weak-field two-photon excitation to the $4s$ state, a π phase jump in the spectral phase can yield either optimal excitation or a nearly dark pulse depending on the position of the phase jump. The dependence on position can be understood in terms of the symmetry of $\Phi(\omega)$ [18]. For strong-field excitation the effect of a π spectral phase jump is best viewed in the time domain. The π spectral jump produces a pair of pulses with a smoothly varying phase which evolves by about π between pulses. Depending on the intensity and pulse spacing, this can result in constructive interference between the contributions of the two pulses (quasi-phase-matching) and optimal transfer, or destructive interference (anti-quasi-phase-matching) and a dark pulse. Note that this is not simply spectral interference. The spectrum of the laser pulse is constant, and so there are no spectral modulations in the pulse as a function of delay as with a Michelson interferometer. Furthermore, in the strong-field

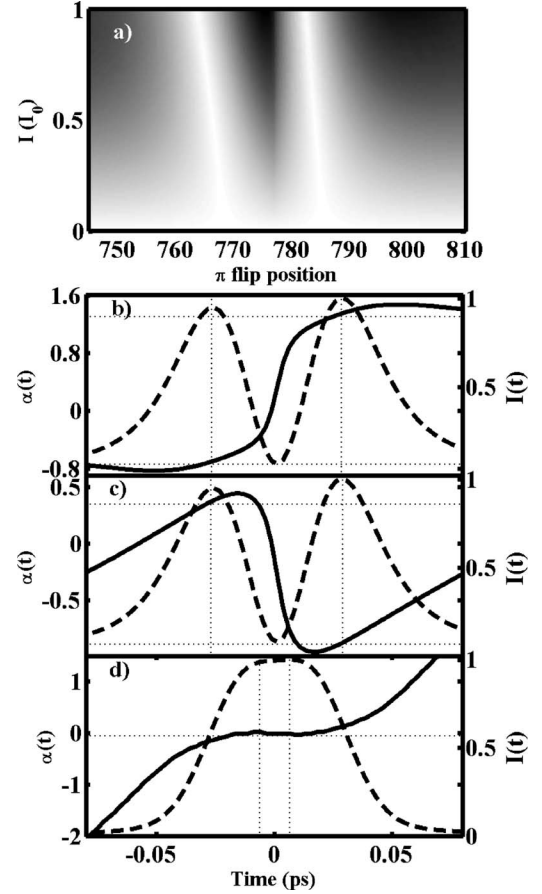


FIG. 5. (a) Calculation of the population transfer using the left-hand side of Eq. (16) as function of peak intensity (for an unshaped pulse) and π flip position. (b), (c), (d) Evolution of $\alpha(t)$ (left axis, solid line) and $I(t)$ (right axis, dashed line) in time for different π phase flip positions (see text). All three are for the same pulse energy, corresponding to the minimum energy required for a π pulse, as defined by Eq. (16) with $\alpha(t)=0$. The straight dotted lines mark the change of $\alpha(t)$ between the two maxima of $I(t)$. In (a) the dark regions correspond to higher population transfer.

limit, the resonance condition is dynamic, meaning that there is no well-defined total frequency to which different combinations of spectral components can add constructively or destructively. As demonstrated below by the variation in population transfer with pulse energy for a given pulse shape, calculations based on a weak-field model using spectral interference [18] do not accurately predict the population transfer achieved by a strong-field laser pulse. Our measurements can be compared directly with [18,20], which were obtained in the weak-field limit. The transition from the weak- to the strong-field regime is highlighted by observing how the population transfer dependence on spectral phase jump position changes with intensity, and the resonance conditions become dynamic.

Figure 4(a) shows the experimental measurement of the $4s$ population following excitation by a pulse with a π spectral phase jump as a function of both pulse energy and phase jump position. Figure 4(b) shows the $4s$ population vs spectral phase jump position for several different intensities. Figures 4(c) and 4(d) show calculations of the $4s$ population

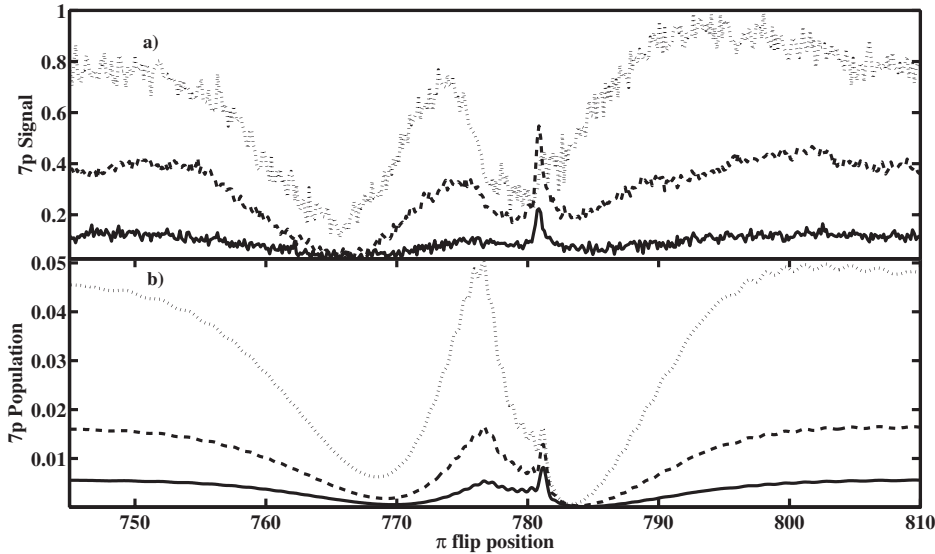


FIG. 6. (a) Measurement of the $7p$ population for three different energies as function of the π flip position. (b) Simulation of the $7p$ population for equivalent peak intensities as function of the π flip position. The enhancement obtained at weak fields at $\lambda_0 = 781.2$ nm washes out for high fields. In all graphs, the solid line is for low intensities $I \approx 0.1I_0$, dashed line is for intermediate energies $I \approx 0.4I_0$, and dotted line is for $I \approx I_0$.

after the same pulses using the Hamiltonian in Eq. (21) for comparison with the experimental results. The calculations agree well with the experimental results at all intensities, with no adjustable parameters. At low intensities, where the DSS is negligible, the measurement reproduces the perturbative results in [18]. However, as the pulse energy increases (and therefore the peak intensity) there are three interesting features to note. One is the shift from right to left of the central peak which corresponds to having the π spectral phase jump on resonance. Another is the growth of this peak above the values far from resonance, and the third is the growth of a new peak at around 800 nm. All three features can be understood in terms of dynamic Stark shifting of the resonance and the integration of the Schrödinger equation using Eq. (15). The shifting of the central peak originally at 777 nm is a direct result of the dynamic Stark shift. As the pulse energy increases, the two-photon resonance shifts to the blue, and it is favorable to have a π phase shift slightly blue detuned from the bare resonance. The growth of the peaks (located at about 777 and 800 nm) above the population transfer for an unshaped pulse can be explained by examining the integral of the off-diagonal terms in Eq. (15). This is illustrated in Fig. 5.

Figure 5(a) shows the integral

$$\int_{-\infty}^{\infty} \chi(t) \exp[i\alpha(t)] dt \quad (27)$$

as a function of intensity and π phase jump position. As expected, this shows agreement with the Fig. 4. The remaining panels show the temporal evolution of the atom-field phase parameter $\alpha(t)$, overlaid with the intensity profile of the pulse. All panels are for an intensity of $I = I_0$. The positions of the spectral phase flip are 775, 781, and 795 nm for Figs. 5(b), 5(c) and 5(d), respectively. These flip positions correspond to the two enhancement peaks and the minimum at 781 nm in the dotted line of Fig. 4(d). For all three cases, the pulse intensity profile corresponds to a pulse pair, as a result of the steplike spectral phase. The graphs show that, if $\alpha(t)$ evolves by roughly either zero or 2π between pulses,

then the population transfer is efficient because the excited-state amplitude from both pulses can add constructively. However, if the evolution of $\alpha(t)$ is closer to π , then there is almost no population transfer because the contributions from the two pulses add destructively. This illustrates how a given pulse parametrization which was originally motivated by frequency-domain considerations for weak-field excitation can be interpreted for the case of strong fields in the time domain using a phase-matching picture.

Figure 6(a) shows the measurements of the $7p$ population transfer as a function of pulse energy and π phase jump position. Figure 6(b) shows simulation results for the dependence on π phase jump position for three different intensities. Again, there is a clear transition from weak to strong fields. A new feature in the measurement which highlights the difference between strong and weak fields is the narrow peak at 781.2 nm. This corresponds to the field-free resonant wavelength for the $4s$ to $7p$ transition [20]. For the lowest intensities, the enhancement with a π flip at this frequency is about a factor of 3 over an unshaped pulse [Fig. 6(b)] consistent with the ratio of 3 seen for weak fields in Fig. 3. However, as the intensity increases, this enhancement essentially disappears as shown in the dashed line in Fig. 6(b). The enhancement vanishes for high field intensities because of the DSSs of the $4s$ and $7p$ states. The resonance condition is not at 781.2 nm at all times during an intense pulse, and averaging over different detunings results in cancellation of this resonant enhancement. We argue that this is a generic feature of strong-field excitation, and control in the strong field must take this into account in order to be effective.

The other features in the $7p$ data follow the $4s$ data, illustrating that the same pulse features that maximize the $4s$ population are efficient at populating the $7p$ as well. We are currently investigating to what extent it is possible to maximize the $7p$ population while minimizing the population of the $4s$. There are several indications that this is possible, and that it is even possible to transfer more population to the $7p$ state than to the $4s$ using strong fields.

In conclusion, we have studied the transition from weak- to strong-field excitation in two- and three-photon transitions using shaped ultrafast laser pulses. The distinction between the two regimes is made in terms of ground-state depletion and dynamic Stark shifts. In weak fields, a frequency-domain picture of the interaction is appropriate and captures the essential atom-field dynamics. In strong fields, the resonance condition becomes dynamic, perturbative strategies for optimizing population transfer break down, and a time-domain

picture yields insight into the strong-field dynamics and pulse shape dependence.

ACKNOWLEDGMENTS

This research was supported by the National Science Foundation under Grant No. 0244748. We gratefully acknowledge helpful discussions with Brett Pearson and Thomas Bergeman.

-
- [1] R. Levis, G. Menkir, and H. Rabitz, *Science* **292**, 709 (2001).
 [2] N. Dudovich, T. Polack, A. Pe'er, and Y. Silberberg, *Phys. Rev. Lett.* **94**, 083002 (2005).
 [3] M. Wollenhaupt, A. Prakelt, C. Sarpe-Tudoran, D. Liese, and T. Baumert, *Appl. Phys. B: Lasers Opt.* **82**, 183 (2006).
 [4] E. Wells, K. J. Betsch, C. W. S. Conover, M. J. DeWitt, D. Pinkham, and R. R. Jones, *Phys. Rev. A* **72**, 063406 (2005).
 [5] I. R. Sola, B. Y. Chang, and H. Rabitz, *J. Chem. Phys.* **119**, 10653 (2003).
 [6] B. J. Sussman, M. Y. Ivanov, and A. Stolow, *Phys. Rev. A* **71**, 051401(R) (2005).
 [7] G. N. Gibson, *Phys. Rev. A* **72**, 041404(R) (2005).
 [8] B. J. Sussman, D. Townsend, M. Y. Ivanov, and A. Stolow, *Science* **314**, 278 (2006).
 [9] R. A. Bartels, T. C. Weinacht, S. R. Leone, H. C. Kapteyn, and M. M. Murnane, *Phys. Rev. Lett.* **88**, 033001 (2002).
 [10] R. Bartels, S. Backus, E. Zeek, L. Misoguti, G. Vdovin, I. P. Christov, M. M. Murnane, and H. C. Kapteyn, *Nature (London)* **406**, 164 (2000).
 [11] R. S. Judson and H. Rabitz, *Phys. Rev. Lett.* **68**, 1500 (1992).
 [12] A. Assion, T. Baumert, M. Bergt, T. Brixner, B. Kiefer, V. Seyfried, M. Strehle, and G. Gerber, *Science* **282**, 919 (1998).
 [13] C. Daniel, J. Full, L. González, C. Lupulescu, J. Manz, A. Merli, Š. Vajda, and L. Wöste, *Science* **299**, 536 (2003).
 [14] R. A. Bartels, M. M. Murnane, H. C. Kapteyn, I. Christov, and H. Rabitz, *Phys. Rev. A* **70**, 043404 (2004).
 [15] D. Cardoza, M. Baertschy, and T. C. Weinacht, *J. Chem. Phys.* **123**, 074315 (2005).
 [16] C. Trallero-Herrero, J. L. Cohen, and T. C. Weinacht, *Phys. Rev. Lett.* **96**, 063603 (2006).
 [17] D. Meshulach and Y. Silberberg, *Nature (London)* **396**, 239 (1998).
 [18] D. Meshulach and Y. Silberberg, *Phys. Rev. A* **60**, 1287 (1999).
 [19] A. Präkelt, M. Wollenhaupt, C. Sarpe-Tudoran, and T. Baumert, *Phys. Rev. A* **70**, 063407 (2004).
 [20] A. Gandman, L. Chuntunov, L. Rybak, and Z. Amitay (unpublished).
 [21] R. R. Jones, *Phys. Rev. Lett.* **74**, 1091 (1995).
 [22] R. R. Jones, *Phys. Rev. Lett.* **75**, 1491 (1995).
 [23] C. Trallero-Herrero, D. Cardoza, T. C. Weinacht, and J. L. Cohen, *Phys. Rev. A* **71**, 013423 (2005).
 [24] S. A. Hosseini and D. Goswami, *Phys. Rev. A* **64**, 033410 (2001).
 [25] N. Dudovich, B. Dayan, S. M. Gallagher Faeder, and Y. Silberberg, *Phys. Rev. Lett.* **86**, 000047 (2001).
 [26] P. Meystre and M. Sargent, *Elements of Quantum Optics*, 3rd ed. (Springer-Verlag, Berlin, 1991).
 [27] Y. Ralchenko, F. C. Jou, D. E. Kelleher, A. E. Kramida, A. Musgrove, J. Reader, W. L. Wiese, and K. Olsen, in *NIST Atomic Spectra Database, NIST Standard Reference Database No. 78* (National Institute of Standards and Technology, Gaithersburg MD, 2006), <http://physics.nist.gov/PhysRefData/ASD/>
 [28] I. I. Sobel'man, *An Introduction to the Theory of Atomic Spectra* (Pergamon Press, Oxford, 1972).
 [29] F. Langhojer, D. Cardoza, M. Baertschy, and T. C. Weinacht, *J. Chem. Phys.* **122**, 014102 (2005).